The Astrophysical Journal Letters, 958:L6 (6pp), 2023 November 20 https://doi.org/10.3847/2041-8213/ad0899

Elusive Iron: Detection of the FeC Radical ($X^3\Delta_i$) in the Envelope of IRC+10216

L. A. Koelemay[1] and L. M. Ziurys[1,2]
[1] Department of Chemistry and Biochemistry, Steward Observatory, University of Arizona, 1305 E. 4th Street Tucson, AZ 85719, USA
[2] Department of Astronomy, Steward Observatory, University of Arizona, 1305 E. 4th Street Tucson, AZ 85719, USA
Received 2023 October 9; revised 2023 October 28; accepted 2023 November 1; published 2023 November 15

Abstract

A new interstellar molecule, FeC ($X^3\Delta_i$), has been identified in the circumstellar envelope of the carbon-rich asymptotic giant branch star IRC+10216. FeC is the second iron-bearing species conclusively observed in the interstellar medium, in addition to FeCN, also found in IRC+10216. The $J = 4 \rightarrow 3$, $5 \rightarrow 4$, and $6 \rightarrow 5$ rotational transitions of this free radical near 160, 201, and 241 GHz, respectively, were detected in the lowest spin–orbit ladder, $\Omega = 3$, using the Submillimeter Telescope of the Arizona Radio Observatory (ARO) for the 1 mm lines and the ARO 12 m at 2 mm. Because the ground state of FeC is inverted, these transitions are the lowest energy lines. The detected features exhibit slight U shapes with LSR velocities near $V_{\rm LSR} \approx -26$ km s^{-1} and linewidths of $\Delta V_{1/2} \approx 30$ km s^{-1}, line parameters characteristic of IRC+10216. Radiative transfer modeling of FeC suggests that the molecule has a shell distribution with peak radius near 300 R_* ($\sim$6″) extending out to $\sim$500 R_* ($\sim$10″) and a fractional abundance, relative to H_2, of $f \sim 6 \times 10^{-11}$. The previous FeCN spectra were also modeled, yielding an abundance of $f \sim 8 \times 10^{-11}$ in a larger shell situated near 800 R_*. These distributions suggest that FeC may be the precursor species for FeCN. Unlike cyanides and carbon-chain molecules, diatomic carbides with a metallic element are rare in IRC+10216, with FeC being the first such detection.

Unified Astronomy Thesaurus concepts: Astrochemistry (75); Evolved stars (481); Circumstellar envelopes (237); Interstellar molecules (849); Radio astronomy (1338); Asymptotic giant branch stars (2100)

1. Introduction

Iron is one of the most relevant elements in astrophysical and astrobiological contexts. It is primarily produced in massive stars that undergo core-collapse and subsequent supernova (SN) explosion (Arnett 1996), releasing the element into the interstellar medium (ISM). A substantial amount is also thought to be generated in Type Ia SNe (Amarsi et al. 2019). Being the most stable product of nucleosynthesis (e.g., Arnett 1996), it is one of more prevalent elements with a cosmic abundance relative to hydrogen of $f \sim 3.2 \times 10^{-5}$ (Asplund et al. 2009). Iron is also one of the most important sources of opacity in the interiors of stars, influencing stellar structure and evolution (e.g., Basu & Antia 2008). Furthermore, it serves as a standard in the determination of stellar metallicity and age, as well as elemental abundances (e.g., Amarsi et al. 2019; Buder et al. 2019). From the viewpoint of astrobiology, iron constitutes a significant portion of the cores of rocky planets, including Earth, specifically in the form of the mineral schreibersite $(Fe, Ni)_3P$ (Hinkel et al. 2020).

Gas-phase iron has been studied extensively in stellar photospheres, H II regions, and planetary nebulae through its atomic lines (e.g., Amarsi et al. 2019). Its abundance and ubiquity suggest that Fe-bearing molecules would be commonly present in interstellar and/or circumstellar gas. Thus far, however, only one such species has been conclusively detected: FeCN. The molecule was observed in the envelope of the carbon-rich asymptotic giant branch (AGB) star, IRC+10216 (Zack et al. 2011). This identification was based on multiple, uncontaminated rotational transitions observed at two separate telescopes. Other searches for iron-bearing molecules (FeO, FeCO) have either been unsuccessful, or tentative, based on a single line (e.g., Kagi et al. 1997; Walmsley et al. 2002; Decin et al. 2018).

The rarity of interstellar Fe-containing molecules could stem from the refractory nature of the element. Iron is known to be depleted in diffuse clouds by as much as 90%, presumably condensed into dust grains (Savage & Sembach 1996; Dwek 2016). Thermodynamic calculations predict that the element condenses out in circumstellar environments as solid iron, FeS, FeSi, and even $(Fe, Ni)_3P$ (Lodders & Fegley 1999), some of which are common in meteoric material (e.g., Pasek 2017). Another obstacle is the lack of accurate rest frequencies for such molecules, as in the case of FeH (Siebert et al. 2020). Nonetheless, the presence of other refractory species such as TiO, VO, and AlNC in stellar envelopes (Kamiński et al. 2013; Ziurys et al. 2002; Humphreys et al. 2019), as well as FeCN, suggest that other iron-bearing molecules may be present in circumstellar gas. FeS and FeO, for example, are predicted by thermochemical equilibrium calculations to be formed (e.g., Agúndez et al. 2020).

One possible molecule for interstellar identification is FeC. The pure rotational spectrum was measured for this free radical in its $X^3\Delta_i$ ground electronic state in the Ziurys group using millimeter-wave direct absorption methods (Allen et al. 1996). Early searches for FeC, however, were not successful, but receiver capabilities have greatly improved since then. Here we report the first astronomical detection of FeC, using the telescopes of the Arizona Radio Observatory (ARO). Critical in these observations was the development of a new, very sensitive 2 mm SIS mixer for the 12 m antenna: see Lauria et al. (2021). FeC has been identified toward IRC+10216 on the basis of three successive rotational transitions measured in the 2 and 1.3 mm bands, as dictated by its inverted ground state. In this Letter, we present our observations and analysis,

and discuss potential formation mechanisms of FeC in circumstellar gas.

2. Observations

The 1.3 mm measurements targeting the $J = 5 \rightarrow 4$ and $J = 6 \rightarrow 5$ lines of FeC at 201 and 241 GHz were made from 2023 February to June using the ARO Submillimeter Telescope (SMT) on Mt. Graham, Arizona. A dual polarization receiver equipped with Atacama Large Millimeter Array (ALMA) Band 6 sideband-separating (SBS) mixers was used, with typical image rejection of $\geqslant$15 dB, intrinsic in the mixer architecture. The backend utilized was a 2048 channel, 1 MHz resolution filterbank, operated in parallel mode. The temperature scale at the SMT is T_A^*, determined by the chopper wheel method, where the radiation temperature is $T_R = T_A^*/\eta_b$. Here η_b is the main beam efficiency, which is 0.70 for the SMT. These observations were averaged with previous data from the 1.3 mm spectral survey of Tenenbaum et al. (2010), yielding spectra with total integration times near 70–90 hr at the respective frequencies. The observations near 201 GHz were somewhat difficult, as they were technically out of the nominal Band 6 range (215–275 GHz) and the mixer performance was somewhat degraded.

The 2 mm observations, which included the $J = 4 \rightarrow 3$ line of FeC at 160 GHz, were conducted with the ARO 12 m telescope on Kitt Peak, Arizona from 2021 November to 2022 April. The receiver employed was dual polarization with SIS mixers, also SBS, developed at ARO. The image rejections were typically $\geqslant$20 dB. The temperature scale for the 12 m is also T_A^*, with $\eta_b = 0.83$. The backend used was the ARO Wideband Spectrometer (AROWS) at 625 kHz resolution and configured with two 4 GHz sections of bandwidth for each receiver channel.

The observations were conducted toward IRC+10216 ($\alpha = 9^h47^m57^s.4$, $\delta = 13°16'43''.6$ (J2000.0)) in beam-switching mode with a subreflector throw of $\pm 2'$. Pointing and focusing were executed every 1.5–2 hr on strong continuum sources such as Jupiter or line pointing on CO. Local oscillator shifts of 10–20 MHz were performed for every transition to identify image contamination. At the SMT, the intermediate frequency was also varied between 5.5 and 7 GHz.

3. Results and Analysis

The electronic ground state of FeC is $X^3\Delta_i$. Consequently, the rotational manifold of this molecule is split into three spin–orbit components, each labeled by the quantum number Ω, where $\mathbf{\Omega} = \mathbf{\Lambda} + \mathbf{\Sigma}$. Here Λ and Σ are the projections of the orbital and electron spin angular momenta along the internuclear axis. In a $^3\Delta_i$ electronic state, $\Lambda = 2$ and $\Sigma = 1$, and therefore $\Omega = 3$, 2, and 1. The state is also inverted, as indicated by the subscript i, such that the $\Omega = 3$ spin–orbit ladder lies lowest in energy, as shown in Figure 1. Each spin–orbit component has its own rotational manifold, labeled by quantum number J. Because J reflects the total angular momentum (excluding nuclear spin), $J \geqslant \Omega$ in each manifold. The total spin–orbit energy splitting is $\pm\Lambda\Sigma A$, such that the individual Ω components are separated by $2A$, where A is the spin–orbit constant ($A \sim 180$ K for FeC; Allen et al. 1996). Therefore, the $\Omega = 1$ and $\Omega = 2$ ladders lie ~720 and 360 K above the $\Omega = 3$ ladder, as shown in Figure 1, and are unlikely to be populated in the envelope of IRC+10216.

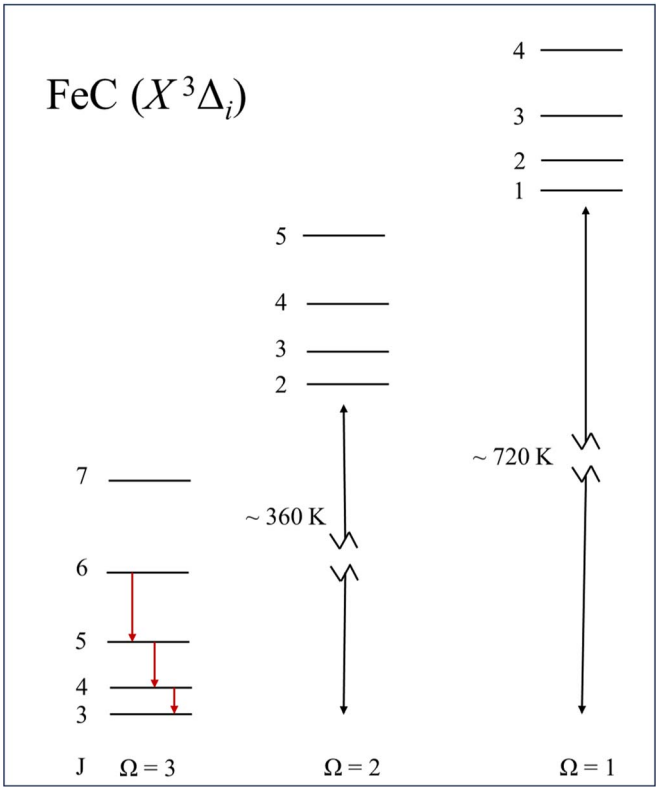

Figure 1. Qualitative energy level diagram of the FeC radical in its ground electronic state ($X^3\Delta_i$). This electronic state consists of three spin ladders, denoted by the quantum number Ω, where $J \geqslant \Omega$, and J defines the total angular momentum excluding nuclear spin. The rotational transitions $J + 1 \rightarrow J$ in the lowest spin ladder of FeC, $\Omega = 3$, observed in this work toward the circumstellar envelope of IRC+10216, are highlighted by red (or gray scale) arrows. The other spin–orbit ladders $\Omega = 2$ and 1 lie higher in energy by ~360 and ~720 K.

The search of FeC was based on the three lowest energy transitions in the $\Omega = 3$ ladder, the $J = 4 \rightarrow 3$, $5 \rightarrow 4$, $6 \rightarrow 5$ lines near 160.6, 200.7, and 240.9 GHz, respectively; see Table 1 and Figure 1. All three transitions were detected with intensities near 1.2–1.5 mK. As shown in the table, these features have the characteristic LSR velocity (~26 km s^{-1}) and linewidth (~30 km s^{-1}) of IRC+10216 (Tenenbaum et al. 2010) and appear to be relatively free from contamination by other spectral lines, including image features. The $J = 7 \rightarrow 6$ line of FeC near 281 GHz was also searched for, but this frequency is out of band for the mixers and had high noise temperatures. After ~100 hr of integration, a noise level comparable to the other frequencies was not achieved. Other molecules were evaluated as potential sources of emission at the FeC frequencies, but none were viable candidates. The integration time required for the transitions were 52, 72, and 91 hr, near 160, 201, and 241 GHz, respectively.

Figure 2 presents the observed spectra of FeC toward IRC +10216. The $J = 4 \rightarrow 3$, $J = 5 \rightarrow 4$ and the $J = 6 \rightarrow 5$ transitions are displayed in the top, middle, and lower panels in the figure. The spectral resolution is 3 km s^{-1} for all three transitions, smoothed from 1.2 km s^{-1} (625 kHz) at 160 GHz, and 1.2–1.5 km s^{-1} (1 MHz) at 201–241 GHz. A linear baseline was removed from all data. The FeC spectra appear slightly U-shaped, consistent with the beam size range of 39″–31″ from 160 to 241 GHz. The inset in each panel shows the same spectrum, overlaid with the model fit (in red or gray

Table 1
Line Parameters for FeC ($X^3\Delta_i$, $\Omega = 3$) in IRC+10216

Transition[a]	Frequency (MHz)	θ_b	T_A^* (mK)	$\Delta V_{1/2}$ (km s^{-1})	V_{LSR} (km s^{-1})
$J = 4 \rightarrow 3$[b]	160590.7889	39.1	1.5 ± 0.3	33 ± 3	-26.5 ± 3
$J = 5 \rightarrow 4$	200729.7762	37.5	1.2 ± 0.4	33 ± 3	-24.6 ± 3
$J = 6 \rightarrow 5$	240862.9510	31.3	1.5 ± 0.2	30 ± 3	-27.1 ± 3

Notes.
[a] Measured with the ARO SMT unless otherwise indicated.
[b] Measured with the ARO 12 m.

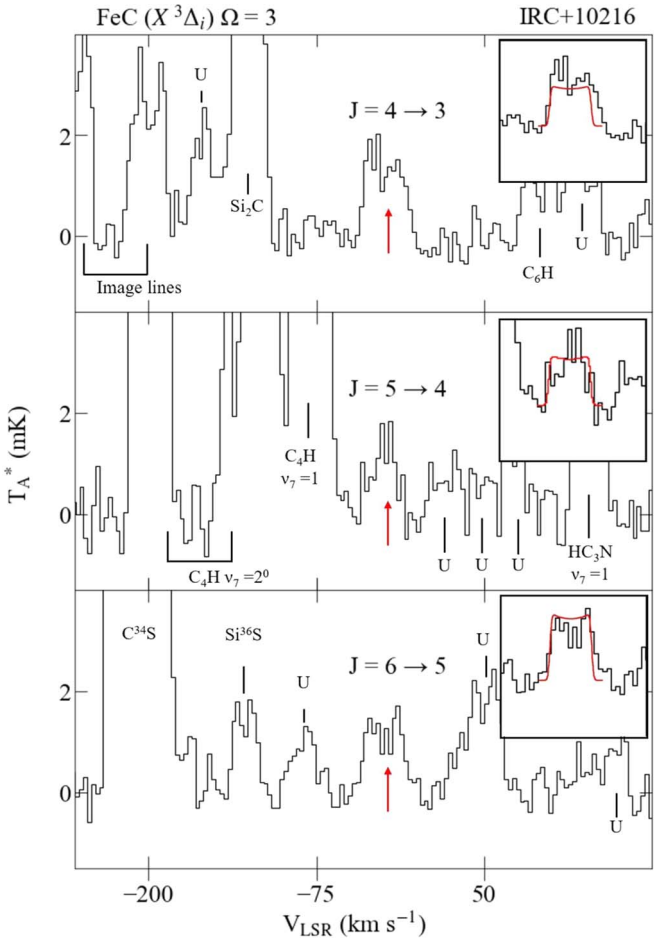

Figure 2. Rotational transitions of FeC ($X^3\Delta_i$) observed toward IRC+10216 using the ARO 12 m and SMT at 2 and 1 mm, respectively. Each spectrum has a spectral resolution of 3 km s^{-1}, smoothed from 1.2 km s^{-1} (0.625 MHz) at 160 GHz, and 1.2–1.5 km s^{-1} (1 MHz) at 201–241 GHz. The temperature scale is T_A^*(mK). The figure shows the $J = 4 \rightarrow 3$ transition near 160 GHz (upper panel), $J = 5 \rightarrow 4$ line near 201 GHz (middle panel), and the $J = 6 \rightarrow 5$ transition near 241 GHz (lower panel), each marked by red (or gray scale) arrows. The inset in each panel shows enlarged versions of each line, with the ESCAPADE-derived fits superimposed (red or gray scale). Integration times are 52, 72, and 91 hr at 160, 201, and 241 GHz, respectively.

scale), as described below. The spectra are dominated by lines of Si_2C, C_4H, and $C^{34}S$, as well as several weak unidentified features, labeled by U.

The spectra of FeC were modeled in order to obtain abundance estimates using the non–local thermodynamic equilibrium (LTE) radiative transfer code ESCAPADE, which was developed by the Ziurys group (Adande et al. 2013). The code calculates molecular line profiles by adjusting the abundance and spatial distribution of a given molecule, assuming a spherical or shell source. Collisions with H_2 and infrared (IR) radiation from dust, modeled as a blackbody at ~500 K (De Beck et al. 2012), are the excitation mechanisms. A mass-loss rate of $3.5 \times 10^{-5}\,M_\odot\,\mathrm{yr}^{-1}$ (Anderson & Ziurys 2014) was assumed for IRC+10216 to set the density profile as a function of r, the distance from the star (e.g., Anderson & Ziurys 2014). The temperature profile is given by the following equation (De Beck et al. 2012):

$$T_K(r) = 400\ \mathrm{K}\left(\frac{2.7 \times 10^{15}}{r}\right)^{1.2}. \quad (1)$$

The envelope expansion velocity was chosen to be $v_{exp} = 14.5$ km s^{-1}; a distance of 130 pc was used. The calculation was begun at 20 R_*, just beyond the dust formation zone (e.g., Agúndez et al. 2012), where $R_* \approx 4 \times 10^{13}$ cm.

Collisional rates for FeC have yet to be determined, and therefore the rates of CS were used, scaled by molecular mass (Schöier et al. 2005). For the IR dust excitation, the $v = 1$ level of FeC was considered, which lies 862.9 cm^{-1} (1242 K) above the ground state (Aiuchi et al. 1999). The experimental dipole moment of FeC is 2.36 D (Steimle et al. 2002), which was used in the modeling. The dipole moment derivative of FeC, which governs the rovibrational transitions, is not known. The dipole derivative was therefore estimated from that of CS, scaled by the relative dipole moments.

Because of the somewhat U-shaped profiles, the radial abundance of FeC was modeled with a shell distribution described by (Adande et al. 2013):

$$f(r) = f_0 \exp\left(-\left(\frac{r - r_{shell}}{r_{outer}}\right)^2\right). \quad (2)$$

In this equation, f_0 denotes the peak fractional abundance relative to H_2, r_{shell} represents the distance from the star where the abundance reaches its maximum f_0, and r_{outer} is the distance from r_{shell} where the abundance decreases by a factor of $1/e$ (Adande et al. 2013; Anderson & Ziurys 2014). For the modeling, the parameters f_0, r_{shell}, and r_{outer} were varied across the ranges 10^{-12}–10^{-9}, 200–1000 R_*, and 100–400 R_*, respectively. All three transitions were modeled simultaneously, and the best fit was determined by a reduced chi-squared analysis, in tandem with visual inspection. The uncertainty of the model is approximately 20%. Modeling was also attempted using a spherical distribution but with less satisfactory results. The modeling results are summarized in Table 2, and the resulting line profiles are shown in the insets in Figure 2 (in red or gray scale), as mentioned.

As a benchmark for the modeling, the abundance of FeC was also estimated using a rotational diagram. Conversion to fractional abundance was done using the H_2 column density as determined by the mass-loss rate (Anderson & Ziurys 2014),

Table 2
Abundances of Fe-bearing Species in IRC+10216[a]

Molecule	Ground State	$f_0(X/H_2)$	Shell Peak (R_*)	Shell Size (R_*)[b]
FeC	$X^3\Delta i$	6×10^{-11}	300	500
FeCN	$X^4\Delta i$	8×10^{-11}	800	1050

Notes.
[a] Assumes a shell distribution.
[b] Outer shell radius where the abundance decreases by $1/e \sim 1/2.7$.

extrapolated over the same range in radius as the ESCAPADE modeling. A rotational temperature was also obtained.

The previous spectra of FeCN were also modeled with ESCAPADE, employing the same input parameters as for FeC. A shell distribution was assumed, as determined by Zack et al. (2011). Three unblended transitions ($J = 13.5 \rightarrow 12.5$, $12.5 \rightarrow 11.5$, and $10.5 \rightarrow 9.5$) at 3 mm were modeled. As with FeC, collisional rates for FeCN were unavailable, and they were therefore scaled from those of HC_3N. Uncertainties for the FeCN modeling are estimated to be 40%.

4. Discussion

4.1. Abundance and Distribution of FeC in IRC+10216

As shown in Figure 2, the radiative transfer modeling reproduced the observed line profiles reasonably well, and also predicted a slight U shape. The analysis suggests that the peak abundance of FeC, relative to H_2, is $f_0 \sim 6 \times 10^{-11}$. The shell distribution of FeC was found to have a maximum at $r_{shell} \sim 300\ R_*$, with $r_{outer} \sim 200\ R_*$, defining a shell outer radius of 500 R_* (2×10^{16} cm). Therefore, the source size for FeC is roughly 21″. From the rotational diagram analysis, $f \sim 3 \times 10^{-11}$ and $T_{rot} \sim 22$ K was calculated for a 21″ source size—in good agreement with the modeling. Notably, the location of the FeC shell is similar to that of another refractory molecule, SiP (Koelemay et al. 2022), which has $r_{shell} \sim 300\ R_*$ and an outer radius of $\sim$550 R_*. Because SiP formation is likely to be associated with dust grain destruction, such processes may apply to FeC as well.

The modeling for FeCN produced an abundance relative to H_2 of $f_0 \sim 8 \times 10^{-11}$ and a shell distribution defined by $r_{shell} \sim 800\ R_*$ and a shell outer radius of $\sim$1050 R_*. These results are also tabulated in Table 2. The fractional abundance derived here for FeCN is a factor of $\sim$2 lower than the value obtained by Zack et al. (2011) for a similar distribution. The abundances are therefore not inconsistent, considering that Zack et al. used an older, less sophisticated code for the modeling.

4.2. Comparison of Metal Carbides with Cyanides

Metal (in the chemist's sense) cyanides are quite common in IRC+10216, being represented by MgNC, AlNC, NaCN, KCN, FeCN, and MgCN (Kawaguchi et al. 1993; Turner et al. 1994; Ziurys et al. 1995, 2002; Pulliam et al. 2010; Zack et al. 2011). In contrast, FeC is the only "metal" carbide thus far observed in this source, or any other object. Two refractory nonmetal carbides are present in IRC+10216, SiC and CP (or PC; Cernicharo et al. 1989; Milam et al. 2008). These two species have abundances of 7×10^{-8} and 1×10^{-8}, respectively. Phosphorus is not nearly as refractory as silicon, such that the best comparison to FeC is SiC. The SiC/FeC ratio is $\sim$1160, which is quite different from the Si/Fe ratio of $\sim$1. SiC may be more prevalent because silicon is readily evaporated from silicon carbide grains under shocked conditions (Bernal et al. 2022). In C-rich envelopes, SiC is thought to be one of the most common grain types (Kwok 2004), and thus can be a good source of gas-phase silicon for molecule formation. An equivalent system is not known for gas-phase iron production, nor for the destruction of Fe-bearing grains.

The radial distributions of both FeC and FeCN are depicted in Figure 3. These species are the only iron-bearing molecules thus far observed in the envelope of IRC+10216. As shown in the figure and Table 2, the abundances of both molecules are within a factor of 1.5 of each other. However, the shell for FeC lies closer to the star, whereas that of FeCN is predominantly in the outer envelope, with a somewhat wider shell. There is overlap between the distributions near 500 R_*.

The overlap observed in the shells of these two molecules indicates a potential correlation between the destruction of FeC and the formation of FeCN. In the outer envelope of IRC +10216, gas-phase chemistry is dominated by photodissociation mechanisms, leading to ion production (Höfner & Olofsson 2018). FeCN might be synthesized from FeC in a process analogous to the creation of NaCN (Turner et al. 1994). The penetrating interstellar UV field may destroy FeC and form Fe^+. Glassgold (1996) predicts that photodestruction can occur for molecules near 300 R_* in IRC+10216, as also found by Anderson & Ziurys (2014) from observations. Once Fe^+ is formed, it can react with HCN, which is known to be present in the outer envelope (Anderson & Ziurys 2014), via the process:

$$Fe^+ + HCN \rightarrow FeCNH^+ + h\nu. \quad (3)$$

FeCN is then produced by electron dissociative recombination.

4.3. Formation of FeC

According to thermodynamic predictions by Lodders & Fegley (1999), the majority of iron in the envelope of a C star will be condensed into dust grains of iron silicide (FeSi), iron metal (Fe), and troilite (FeS). At a pressure of 10^{-4} bar, which is typical for the dust condensation zone of a circumstellar envelope, these minerals exhibit condensation temperatures of approximately 1100, 1350, and 700 K (Ferrarotti et al. 2000; Lodders 2003). However, this condensation chemistry requires LTE conditions, which may be altered by thermal pulsing on the AGB, which creates shocks (Marigo et al. 2016). These shocks disrupt grain formation, keeping some refractory material in the gas phase. The presence of gas-phase atomic metals Al, Ca, and Fe in the envelope of IRC+10216 has been proven by Mauron & Huggins (2010), who observed atomic lines of these elements against a background star. Therefore, some iron must remain in the gas phase, leading to Fe-bearing molecules. Unfortunately, there are virtually no known rates for reactions of iron-containing species, making formation processes speculative.

In analogy to the formation of SiC, one possible pathway to FeC is through iron hydride:

$$FeH + C \rightarrow FeC + H. \quad (4)$$

The estimated rate for the formation of SiC through this pathway is $k \sim 6.6 \times 10^{-11}$ cm^3 s^{-1} (Wakelam et al. 2012), which is favorable. Another analog process creating FeC would

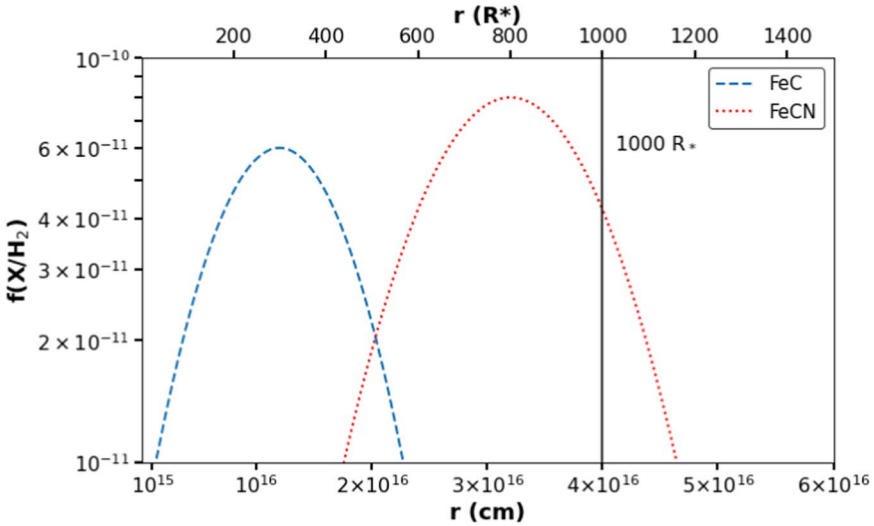

Figure 3. Radial abundance profiles for FeC (blue, dashed) and FeCN (red, dots) within the envelope of IRC+10216, derived from the model fitting, plotted as a function of distance from the star (in cm or R_*). The abundances are shown in log scale. The black solid line marks a radius of 1000 R_*. The FeC distribution is closer to the star than that of FeCN, with some overlap, suggesting the cyanide forms from the carbide through photochemistry.

involve FeC_2 destruction by O atoms:

$$FeC_2 + O \rightarrow FeC + CO. \quad (5)$$

Here the rate with SiC_2 is $k \sim 4 \times 10^{-11}\,cm^3\,s^{-1}$, which is also favorable. However, FeC_2 is not a known interstellar molecule, and there is limited experimental and theoretical data on this species. Other processes leading to SiC involve dissociation recombination reactions of larger Si-bearing ions, but again, for which iron analogs are not known. Another possible precursor is Fe_3C, a predicted iron condensate in C-rich envelopes (Agúndez et al. 2020). The formation of FeC in IRC+10216 is currently unclear and warrants further investigation.

There are likely to be other iron-containing molecules in IRC +10216. A slew of magnesium-bearing molecules has recently been identified in this source, including MgCCH, MgC_2, MgC_4H (Agúndez et al. 2014; Cernicharo et al. 2019; Changala et al. 2022). This substantial list suggests that species such as FeCCH, FeC_2, and FeC_4H may be present in circumstellar gas, although iron is more refractory than magnesium, and the chemistry may be different. Rotational rest frequencies for such species are currently not available. The detection of FeC suggests that more laboratory spectroscopy of Fe-bearing molecules is certainly needed.

Acknowledgments

This research is supported by NSF Grants AST-1907910 and AST-2307305. The authors thank the Arizona Radio Observatory staff, especially G. Lauria for outstanding mixer development.

ORCID iDs

L. A. Koelemay https://orcid.org/0000-0001-9334-3149
L. M. Ziurys https://orcid.org/0000-0002-1805-3886

References

Adande, G. R., Edwards, J. L., & Ziurys, L. M. 2013, ApJ, 778, 22
Agúndez, M., Cernicharo, J., & Guélin, M. 2014, A&A, 570, A45
Agúndez, M., Fonfría, J. P., Cernicharo, J., et al. 2012, A&A, 543, A48
Agúndez, M., Martínez, J. I., de Andres, P. L., Cernicharo, J., & Martín-Gago, J. A. 2020, A&A, 637, A59
Aiuchi, K., Tsuji, K., & Shibuya, K. 1999, CPL, 309, 229
Allen, M. D., Pesch, T. C., & Ziurys, L. M. 1996, ApJL, 472, L57
Amarsi, A. M., Nissen, P. E., & Skúladóttir, Á. 2019, A&A, 630, A104
Anderson, J. K., & Ziurys, L. M. 2014, ApJL, 795, L1
Arnett, D. 1996, Supernovae and Nucleosynthesis: An Investigation of the History of Matter, from the Big Bang to the Present (Princeton Univ. Press: Princeton)
Asplund, M., Grevesse, N., Jacques Sauval, A., & Scott, P. 2009, ARA&A, 47, 481
Basu, S., & Antia, H. M. 2008, PhR, 457, 217
Bernal, J. J., Zega, T. J., & Ziurys, L. M. 2022, JPCA, 126, 5761
Buder, S., Lind, K., Ness, M. K., et al. 2019, A&A, 624, A19
Cernicharo, J., Cabezas, C., Pardo, J. R., et al. 2019, A&A, 630, L2
Cernicharo, J., Gottlieb, C. A., Guélin, M., Thaddeus, P., & Vrtilek, J. M. 1989, ApJL, 341, L25
Changala, P. B., Gupta, H., Cernicharo, J., et al. 2022, ApJL, 940, L42
De Beck, E., Lombaert, R., Agúndez, M., et al. 2012, A&A, 539, A108
Decin, L., Danilovich, T., Gobrecht, D., et al. 2018, ApJ, 855, 113
Dwek, E. 2016, ApJ, 825, 136
Ferrarotti, A., Gail, H.-P., Degiorgi, L., & Ott, H. R. 2000, A&A, 357, L13
Glassgold, A. E. 1996, ARA&A, 34, 241
Hinkel, N. R., Harnett, H. E., & Young, P. A. 2020, ApJL, 900, L38
Höfner, S., & Olofsson, H. 2018, A&ARv, 26, 1
Humphreys, R. M., Ziurys, L. M., Bernal, J. J., et al. 2019, ApJL, 874, L26
Kagi, E., Kasai, Y., Ungerechts, H., & Kawaguchi, K. 1997, ApJ, 488, 776
Kamiński, T., Gottlieb, C. A., Menten, K. M., et al. 2013, A&A, 551, A113
Kawaguchi, K., Kagi, E., Hirano, T., Takano, S., & Saito, S. 1993, ApJL, 406, L39
Koelemay, L. A., Burton, M. A., Singh, A. P., et al. 2022, ApJL, 940, L11
Kwok, S. 2004, Natur, 430, 985
Lauria, E. F., Reiland, G. P., Lichtenberger, A. W., Kerr, A. R., & Ziurys, L. M. 2021, URSL, 3, 1
Lodders, K. 2003, ApJ, 591, 1220
Lodders, K., & Fegley, B., Jr 1999, in IAU Symp. 191, Asymptotic Giant Branch Stars, ed. T. Le. Bertre, A. Lébre, & C. Waelkens (San Francisco, CA: ASP), 279
Marigo, P., Ripamonti, E., Nanni, A., Bressan, A., & Girardi, L. 2016, MNRAS, 456, 23
Mauron, N., & Huggins, P. J. 2010, A&A, 513, A31
Milam, S. N., Halfen, D. T., Tenenbaum, E. D., et al. 2008, ApJ, 684, 618
Pasek, M. 2017, GeoFr, 8, 329
Pulliam, R. L., Savage, C., Agúndez, M., et al. 2010, ApJL, 725, L181
Savage, B. D., & Sembach, K. R. 1996, ARA&A, 34, 279
Schöier, F. L., van der Tak, F. F. S., van Dishoeck, E. F., & Black, J. H. 2005, A&A, 432, 369

Siebert, M. A., Simon, I., Shingledecker, C. N., et al. 2020, ApJ, 901, 22
Steimle, T. C., Virgo, W. L., & Hostutler, D. A. 2002, JChPh, 117, 1511
Tenenbaum, E. D., Dodd, J. L., Milam, S. N., Woolf, N. J., & Ziurys, L. M. 2010, ApJS, 190, 348
Turner, B. E., Steimle, T. C., & Meerts, L. 1994, ApJL, 426, L97
Wakelam, V., Herbst, E., Loison, J.-C., et al. 2012, ApJS, 199, 21
Walmsley, C. M., Bachiller, R., Pineau des Foréts, G., & Schilke, P. 2002, ApJL, 566, L109
Zack, L. N., Halfen, D. T., & Ziurys, L. M. 2011, ApJL, 733, L36
Ziurys, L. M., Apponi, A. J., Guélin, M., & Cernicharo, J. 1995, ApJL, 445, L47
Ziurys, L. M., Savage, C., Highberger, J. L., et al. 2002, ApJL, 564, L45